

# Thermo-acoustic Sound Generation in the Interaction of Pulsed Proton and Laser Beams with a Water Target

R. Lahmann<sup>a,\*</sup>, G. Anton<sup>a</sup>, K. Graf<sup>a</sup>, J. Hößl<sup>a</sup>, A. Kappes<sup>a</sup>, U. Katz<sup>a</sup>, K. Mecke<sup>b</sup>, S. Schwemmer<sup>c,1</sup>

<sup>a</sup>Erlangen Centre for Astroparticle Physics (ECAP), Friedrich-Alexander-Universität Erlangen-Nürnberg, Erwin-Rommel-Str. 1, 91058 Erlangen, Germany

<sup>b</sup>Institut für Theoretische Physik, Friedrich-Alexander-Universität Erlangen-Nürnberg, Staudtstr. 7, 91058 Erlangen, Germany

<sup>c</sup>Landessternwarte, Königstuhl 12, 69117 Heidelberg, Germany (formerly at ECAP)

## Abstract

The generation of hydrodynamic radiation in interactions of pulsed proton and laser beams with matter is explored. The beams were directed into a water target and the resulting acoustic signals were recorded with pressure sensitive sensors. Measurements were performed with varying pulse energies, sensor positions, beam diameters and temperatures. The obtained data are matched by simulation results based on the thermo-acoustic model with uncertainties at a level of 10%. The results imply that the primary mechanism for sound generation by the energy deposition of particles propagating in water is the local heating of the medium. The heating results in a fast expansion or contraction and a pressure pulse of bipolar shape is emitted into the surrounding medium. An interesting, widely discussed application of this effect could be the detection of ultra-high energetic cosmic neutrinos in future large-scale acoustic neutrino detectors. For this application a validation of the sound generation mechanism to high accuracy, as achieved with the experiments discussed in this article, is of high importance.

**Keywords:** cosmic neutrinos, acoustic neutrino detection, thermo-acoustic model, ultra-high energy cosmic rays, beam interaction  
**PACS:**

## 1. Introduction

In 1957 G.A. Askaryan pointed out that ionisation and cavitation along a track of an ionising particle through a liquid leads to hydrodynamic radiation [1]. In the 1960s, 1970s and 1980s, theoretical and experimental studies have been performed on the hydrodynamic radiation of beams and particles traversing dense media [2–8].

The interest in characterising the properties of the acoustic radiation was, among other reasons, lead by the idea that the effect can be utilised to detect ultra-high energy ( $E \gtrsim 10^{18}$  eV) cosmic, i.e. astrophysical neutrinos, in dense media like water, ice and salt. In the 1970s this idea was discussed within the DUMAND optical neutrino detector project [9] and has been studied in connection with Cherenkov neutrino detector projects since. The detection of such neutrinos is considerably more challenging than the search for high-energy neutrinos ( $E \gtrsim 10^{10}$  eV) as currently pursued by under-ice and underwater Cherenkov neutrino telescopes [10–12]. Due to the low expected fluxes, detector sizes exceeding  $100 \text{ km}^3$  are needed [13]. However, the properties of the acoustic method allow for sparsely instrumented arrays with  $\sim 100$  sensors/ $\text{km}^3$ .

To study the feasibility of a detection method based on acoustic signals it is necessary to understand the properties of

the sound generation by comparing measurements and simulations based on theoretical models. According to the so-called thermo-acoustic model [2], the energy deposition of particles traversing liquids leads to a local heating of the medium which can be regarded as instantaneous with respect to the hydrodynamic time scales. Due to the temperature change the medium expands or contracts according to its bulk volume expansion coefficient  $\alpha$ . The accelerated motion of the heated medium generates an ultrasonic pulse whose temporal signature is bipolar and which propagates in the volume. Coherent superposition of the elementary sound waves, produced over the cylindrical volume of the energy deposition, leads to a propagation within a flat disk-like volume in the direction perpendicular to the axis of the particle shower.

In this study, the hydrodynamic signal generation by two types of beams, interacting with a water target, was investigated: pulsed protons and a pulsed laser, mimicking the formation of a hadronic cascade from a neutrino interaction under laboratory conditions. With respect to the aforementioned experimental studies of the thermo-acoustic model, the work presented here can make use of previously unavailable advanced tools such as GEANT4 [14] for the simulation of proton-induced hadronic showers in water. Good agreement was found in the comparison of the measured signal properties with the simulation results, providing confidence to apply similar simulation methods in the context of acoustic detection of ultra-high energy neutrinos. A puzzling feature observed in previous studies—a non-vanishing signal amplitude at a temperature of

\*Corresponding author

Email address: robert.lahmann@physik.uni-erlangen.de (R. Lahmann)

Lahmann)

<sup>1</sup>formerly at ECAP

4°C, where for water at its highest density no thermo-acoustic signal should be present—was investigated in detail. Such a residual signal was also observed for the proton beam experiment described in this article, but not for the laser beam, indicating that the formation of this signal is related to the charge or the mass of the protons.

## 2. Derivation of the Model

In the following, the thermo-acoustic model [2, 3] is derived from basic assumptions, using a hydrodynamic approach. Basis is the momentum conservation, i.e., the Euler Equation

$$\frac{\partial(\rho v_i)}{\partial t} = - \sum_{j=1}^3 \frac{\partial \Pi_{ij}}{\partial x_j}, \quad (1)$$

for mass density  $\rho$ , velocity vector field of the medium  $(v_1, v_2, v_3)$  and momentum-density tensor

$$\Pi_{ij} = p\delta_{ij} + \rho v_i v_j \quad (2)$$

including the pressure  $p$  [15]. Equation (1) can be derived from momentum conservation. In the derivation, energy dissipation resulting from processes such as internal friction or heat transfer are neglected. Motions described by the Euler Equation hence are adiabatic. Taking the three partial derivatives of Eq. (1) with respect to  $x_i$  and using for the density the continuity equation

$$\frac{\partial \rho}{\partial t} + \sum_{i=1}^3 \frac{\partial}{\partial x_i}(\rho v_i) = 0, \quad (3)$$

a non-linear wave equation can be derived:

$$\frac{\partial^2 \rho}{\partial t^2} = \sum_{i,j=1}^3 \frac{\partial^2 \Pi_{ij}}{\partial x_i \partial x_j}. \quad (4)$$

To solve this equation, the problem is approached in two separated spatial regions: Firstly, a region  $B$  ('beam'), where the energy is deposited in the beam interactions with the fluid and thus the wave excited in a non-equilibrium process; and secondly, a hydrodynamic ('acoustic') region  $A$ , where the acoustic wave propagates through the medium and where linear hydrodynamics in local equilibrium can be assumed. This splitting can be reflected by the momentum density tensor, rewriting it as

$$\Pi_{ij}(\vec{r}) = \begin{cases} \Pi_{ij}^A(\vec{r}) & \text{for } \vec{r} \in A \\ \Pi_{ij}^B(\vec{r}) & \text{for } \vec{r} \in B \end{cases}. \quad (5)$$

In local equilibrium the changes in mass density are given by

$$\begin{aligned} d\rho &= \left. \frac{\partial \rho}{\partial p} \right|_{S,N} dp + \left. \frac{\partial \rho}{\partial S} \right|_{p,N} dS \\ &= \frac{1}{v_s^2} dp - \frac{\alpha}{c_p} \frac{\delta Q}{V} \end{aligned} \quad (6)$$

with the bulk volume expansion coefficient  $\alpha = -\frac{1}{\rho} \left. \frac{\partial \rho}{\partial T} \right|_{p,N}$ , the energy deposition  $\delta Q = T dS$ , the adiabatic speed of sound  $v_s$  in the medium and the specific heat  $c_p = \frac{T}{N} \left. \frac{\partial S}{\partial T} \right|_{p,N}$ .

In the acoustic regime, where  $\delta Q = 0$ , the momentum density tensor can be expressed as  $\Pi_{ij}^A = p\delta_{ij} = v_s^2 \rho \delta_{ij}$  (using Eqs. (2) and (6)), where we assume an adiabatic density change with pressure. The non-linear kinetic term  $\rho v_i v_j$  entering  $\Pi_{ij}^A$ , according to Eq. (2) can be neglected for small deviations  $\rho' = \rho - \rho_0$  from the static density  $\rho_0$  and small pressure differences  $p' = p - p_0$  from the static pressure  $p_0$  [15].

In the region  $B$ , where non-equilibrium deposition occur, one may make the *ansatz*

$$\Pi_{ij}^B = p\delta_{ij} + \beta u_i u_j \quad (7)$$

with the direction  $u_i$  of the beam which breaks the isotropy of the energy-momentum tensor and describes with the parameter  $\beta$  in an effective way the momentum transfer on the fluid.

Although in non-equilibrium we apply Eq. (6) with the energy deposition density  $\epsilon \equiv Q/V$  of the beam. Then, with the additional energy-momentum tensor due to the beam

$$\delta \Pi_{ij}^B := v_s^2 \frac{\alpha}{c_p} \epsilon \delta_{ij} + \beta u_i u_j$$

the wave equation (4) reads

$$\vec{\nabla}^2 p' - \frac{1}{v_s^2} \frac{\partial^2 p'}{\partial t^2} = - \sum_{i,j=1}^3 \frac{\partial^2 \delta \Pi_{ij}^B}{\partial x_i \partial x_j} \quad (8)$$

The general solution for the wave equation can be written using a Green function approach as

$$\begin{aligned} p'(\vec{r}, t) &= \frac{1}{4\pi} \sum_{i,j=1}^3 \int_B dV' \frac{1}{|\vec{r} - \vec{r}'|} \frac{\partial^2 \delta \Pi_{ik}^B(\vec{r}', t')}{\partial x'_i \partial x'_k} \\ &= \frac{1}{4\pi} \int_B dV' \left[ \frac{n_i n_k}{|\vec{r} - \vec{r}'|} \frac{\partial^2 \delta \Pi_{ik}^B(\vec{r}', t')}{v_s^2 \partial t'^2} \right. \\ &\quad \left. + \frac{3n_i n_k - \delta_{ik}}{|\vec{r} - \vec{r}'|^2} \left( \frac{\partial \delta \Pi_{ik}^B(\vec{r}', t')}{v_s \partial t'} + \frac{\delta \Pi_{ik}^B}{|\vec{r} - \vec{r}'|} \right) \right] \end{aligned} \quad (9)$$

with the components of the unit vector  $n_i = (x_i - x'_i)/|\vec{r} - \vec{r}'|$  and the retarded time  $t' = t - |\vec{r} - \vec{r}'|/v_s$ . For the last conversion, partial integration and the total derivative  $\frac{d}{dx_i} = \frac{\partial}{\partial x_i} + \frac{1}{v_s} \frac{\partial}{\partial t}$  have been used repeatedly. Note that  $\delta \Pi_{ij}^B = 0$  for  $\vec{r} \in A$ , so that the integration is carried out over the volume of the energy deposition region  $B$ .

Assuming an energy deposition without momentum transfer to the medium, the kinetic term in the *ansatz* (7) can be neglected ( $\beta = 0$ ) yielding

$$p'(\vec{r}, t) = \frac{1}{4\pi} \frac{\alpha}{c_p} \int_V \frac{dV'}{|\vec{r} - \vec{r}'|} \frac{\partial^2}{\partial t'^2} \epsilon(\vec{r}', t') \quad (10)$$

for a thermo-acoustic wave generated solely by heating of the medium. The signal amplitude  $p'$  can be shown to be proportional to the dimensionless quantity  $v_s^2 \alpha / c_p$  when solving Eq. (10) for the case of an instantaneous energy deposition.

Equation (10) is equivalent to the results obtained from the approaches presented in [2, 3]. The derivation pursued above, however, uses a different approach starting with the Euler equation and an anisotropic energy-momentum tensor, yielding a

more general expression in Eq. (9). Only if assuming an isotropic energy deposition one arrives at the expression for the pressure deviation  $p'$  given in Eq. (10).

Note that the validation of the last assumption  $\beta = 0$  being a good approximation would require a detailed knowledge of the momentum transfer from the beam to the medium. Taking it into account would result in an additional dipole term  $\sim \ddot{\beta}(\vec{u} \cdot \vec{n})^2$  in Eq. (10) which may become the dominant contribution to wave generation if  $\alpha \approx 0$  close to  $4.0^\circ\text{C}$ . However, for  $\beta = 0$  the pressure field resulting from a beam interaction in a medium is determined by the spatial and temporal distribution of the energy deposition density  $\epsilon$  alone. The amplitude of the resulting acoustic wave is governed by the thermodynamic properties  $v_s$ ,  $c_p$  and  $\alpha$ , the latter three depending primarily on the temperature of the medium. A controlled variation of these parameters in the conducted laboratory experiments and a study of the resulting pressure signals therefore allows for a precise test of the thermo-acoustic model.

Simulations based on the thermo-acoustic model, as performed to interpret the results of the experiments described in the next section, will be discussed in Sec. 5. Note that the energy deposition density  $\epsilon$  and its temporal evolution for the proton and laser beam interactions discussed in this paper are quite different from those expected for the interaction of ultra-high energy neutrinos. However, if a simulation starting from basic principles allows for a good reproduction of the experimental results, it is reasonable to assume that these simulation methods are transferable to neutrino interactions, as they are governed by the same underlying physical processes.

### 3. Experimental Setup and Beam Characteristics

The experiments presented in this paper were performed with a pulsed infrared Nd:YAG laser facility ( $\lambda = 1064 \text{ nm}$ ) located at the Erlangen Centre for Astroparticle Physics (ECAP) of the University of Erlangen, and the pulsed 177 MeV proton beam of the ‘‘Gustaf Werner Cyclotron’’ at the ‘‘Theodor Svedberg Laboratory’’ in Uppsala, Sweden. The beam properties allow for a compact experimental setup. In both cases, the beams were dumped into a dedicated  $150 \times 60 \times 60 \text{ cm}^3$  water tank, where the acoustic field was measured with several position-adjustable acoustic sensors (see Fig. 1). The sensors (also called hydrophones) could be positioned within the tank with absolute uncertainties below 1 cm. The temperature of the water could be varied between  $1^\circ\text{C}$  and  $20^\circ\text{C}$  with a precision of  $0.1^\circ\text{C}$ . The temperature was brought to a particular value by first cooling the water with ice; subsequently the whole water volume was heated to the desired temperature in a controlled, gradual procedure. Once the water temperature had been established, at least 10 min remained for measurements until the water volume heated up by  $0.1^\circ\text{C}$  through heat transfer from the environment. This time span was sufficient for all measurements conducted at water temperatures below the ambient temperature.

The explored range of spill energies for the proton beam was from 10 PeV to 410 PeV, the beam diameter was approximately 3 mm and the spill time  $t_s \approx 30 \mu\text{s}$ . For 177 MeV protons, the energy deposition in the water along the beam axis ( $z$ -axis,

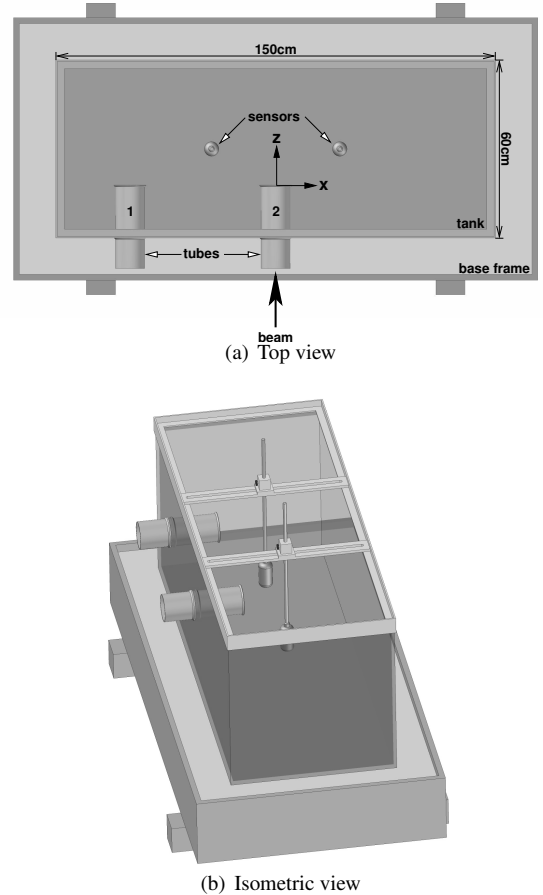


Figure 1: Schematic view of the experimental setup. Beams can enter the water volume through a thin foil (proton beam) or glass window (laser beam), which are set away from the tank walls via an air-filled tube to minimise effects of surface reflections on the recorded signals. Either of the two tubes, labelled ‘1’ and ‘2’ in (a) was used, depending on the experimental setup. The origin of the coordinate system was chosen at the entry point of the beam into the water target, see example in (a).

beam entry into the water at  $z = 0 \text{ cm}$ ) is relatively uniform up to  $z = 20 \text{ cm}$  ending in the prominent Bragg-peak at  $z \approx 22 \text{ cm}$  (see Fig. 2). To adjust the spill energy, the number of protons per bunch was varied. The total charge of a bunch was calibrated with two independent methods (Faraday cups and scintillation counters), leading to an uncertainty on the order of 15%, with some higher values for low spill energies. To obtain the beam intensity and profile for the proton interactions in the water tank, the distance of about 1.2 m that the beam was travelling from the exit of the beam pipe through air and its entering into the water tank were included in the GEANT4 simulation.

For the laser experiment, the pulse energy was adjusted between 0.1 EeV and 10 EeV and calibrated using a commercial power meter. The beam had a diameter of approximately 2 mm and the pulse length was fixed at 9 ns. For the infrared light used, the laser energy density deposited along the beam axis has an exponential decrease with an absorption length of  $(5.9 \pm 0.1) \text{ cm}$  (see Fig. 2).

For both beam types the lateral energy deposition profile was

Gaussian (the aforementioned beam diameters are the  $\sigma$ 's of the profiles). The two experiments allow to explore different spatial and temporal distributions of the energy deposition as well as two different mechanisms of energy transfer into the medium. For both beams, energy is deposited via excitation, in addition the medium is ionised in the case of the proton beam.

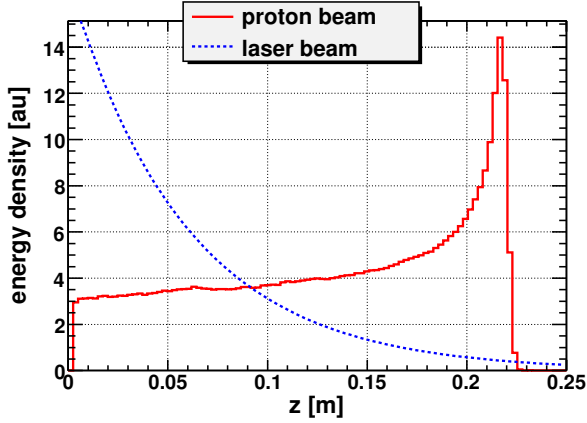


Figure 2: Simulated energy deposition density along the beam axis ( $z$ -axis) for the two beam types (integral normalised to 1). For the proton beam the Bragg peak is prominent at 0.22 m, for the laser beam the decrease is exponential with an attenuation length of 0.059 m.

For the signal recording, sensors based on the piezo-electric effect [18] were used. A full characterisation of these sensors had been performed prior to the experiments. They are linear in amplitude response, the frequency response is flat starting from a few kHz up to the main resonance at 40 kHz with a sensitivity of  $-155$  dB re  $1\text{V}/\mu\text{Pa}$  ( $\sim 0.02$  V/Pa). The main resonance is more sensitive by  $\sim 5$  dB re  $1\text{V}/\mu\text{Pa}$  and sensitivity drops rapidly at higher frequencies; at 90 kHz, the sensitivity has dropped by 20 dB. The absolute uncertainty in the determination of the sensitivity is at a level of 2 dB in the frequency range of interest. Above 90 kHz the uncertainty exceeds 5 dB. To calculate the response of the sensors to an external pressure pulse a parametrised fit of an equivalent circuit model as described in [18] was used. The sensitivity dependence on temperature was measured and the relative decrease was found to be less than 1.5% (or about 0.13 dB) per  $1^\circ\text{C}$ .

For every set of fixed experimental parameters (temperature, energy, sensor position, etc.) the signals of 1000 beam pulses were recorded with a digital oscilloscope at a sampling rate in excess of 1 MHz. This rate is sufficient for the signals with spectral components up to 100 kHz, where the sensitivity of the sensors is negligibly small. These individual pulses were averaged to reduce background and environmental noise in the analysis, thereby obtaining a very high statistical precision.

#### 4. Basic Features of the Measured Signals

Figure 3 shows typical signals measured in the proton and the laser experiment, respectively, using the same sensors and experimental setup. The general shapes of the two signals differ:

a typical signal for the proton beam shows a bipolar signature<sup>2</sup>, the one for the laser deviates from such a generic form. The laser signal has high frequency components up to several MHz due to the high energy deposition density at the point of beam entry and the almost instantaneous energy deposition compared to the  $\mu\text{s}$  pulse of the proton beam; therefore the resonance of the sensor is excited causing a ringing in the measured signal. The spatial distribution of the energy density  $\epsilon$  deposited by the laser leads to the two separate signals: the first originates in the beam area at the same  $z$ -region as the sensor placement (*'direct signal'*), the second from the beam entry, a point of discontinuity where most of the energy is deposited (*'beam entry signal'*).

The signal of the proton beam is deteriorated with respect to an ideal bipolar signal. Three main contributions to this distortion can be discerned: the recorded signal starts before the expected onset of the acoustic signal ( $55.2$   $\mu\text{s}$  for the given position, see Fig. 3, given by the sonic path length); reflections of the acoustic wave on the beam entry window overlay the original wave starting in the first rarefaction peak; and finally there are frequency components of the signal exciting a resonant response of the sensor, slightly changing the signal shape and causing ringing. The first point was studied and found to be consistent with an electric charge effect in the sensors caused by the proton beam. Its starting time was always coincident with the beam pulse entry into the water, even for sensor distances of up to 1 m, hinting at an electromagnetic origin of the distorting signal. The shape of this non-acoustic signal is consistent with the integrated time-profile of the beam pulse with a subsequent exponential decay. This deformation of the main signal is considered a systematic uncertainty on the signal properties and treated as such in the analysis. For the most part, its shape was fitted and subtracted from the signal.

In order to minimise the impact of the signal deformation caused by the described effects on the analysis of the recorded signals, robust characteristics were used: the peak-to-peak amplitude and the signal length from maximum to minimum of the signal. For the laser experiment these features were extracted for the direct signals only.

#### 5. Simulation of Thermo-Acoustic Signals

For an in-depth validation of the thermo-acoustic model, comparisons of the signal properties with simulation results based on the model are essential. To this end, a simulation of the expected signals was developed. It is based on the thermo-acoustic model using a numeric solution of Eq. (10). The input parameters to the simulation were either measured at the experiments, i.e. medium temperature and beam profiles, or simulated, i.e. the energy deposition of the protons (using GEANT4). The thermodynamic parameters bulk volume expansion coefficient, heat capacity and speed of sound were derived from the measured water temperature using standard parametrisations. Tap water quality was assumed.

<sup>2</sup>Note that also the expected signal shape for acoustic pulses produced in interactions of ultra-high energy neutrinos in water is a bipolar one [17].

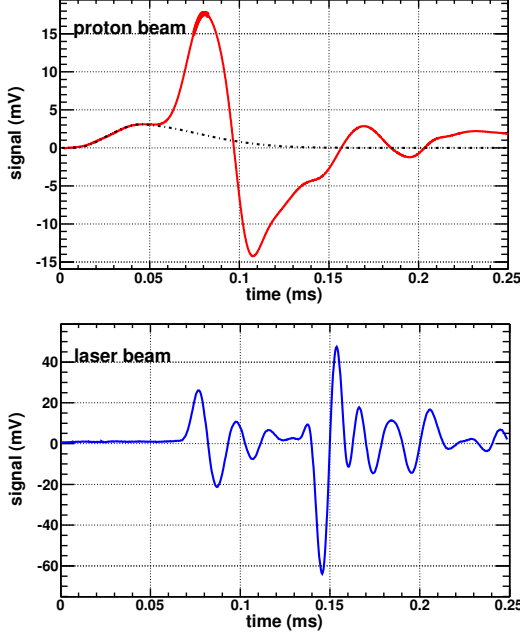


Figure 3: Typical signals measured in the proton (upper graph) and laser (lower graph) experiment. Both signals (solid lines) were taken at a sensor position near  $x=10$  cm and  $z=20$  cm and are shown within the same time interval. The dash-dotted line in the upper graph indicates the charge effect described in the text.

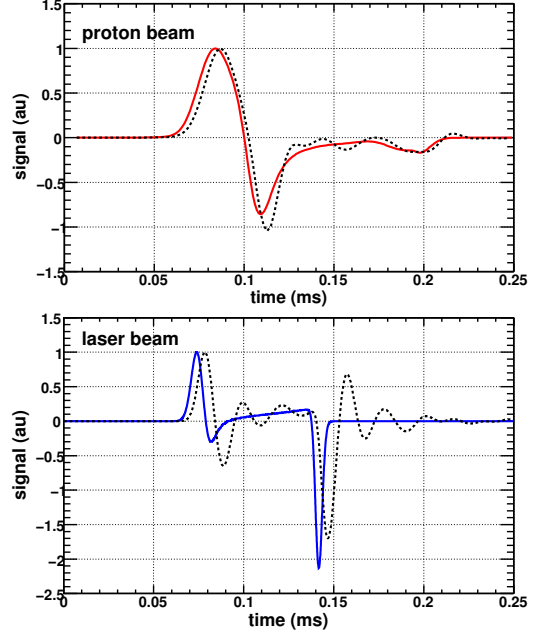


Figure 4: Simulated signals for the proton (upper graph) and laser experiment (lower graph). Both signals (solid lines) were calculated for the experimental conditions of Fig. 3. The corresponding dashed-lined signals mark the simulated signals after convolution with the sensor response. For better comparability, the signal maxima were normalised to 1.

A series of simulations was conducted, where the input parameters were varied individually in the range given by the experiment, including uncertainties. Especially the spatial and temporal beam profile have a substantial impact on amplitude, duration and shape of the signal. Simulated signals and the respective sensor response corresponding to the measured signals of Fig. 3 are shown in Fig. 4. To minimise systematic effects from the setup caused e.g. by reflections on the surfaces, the sensor response was convoluted onto the simulated signals, rather than deconvoluted from the measured ones. Thus in the analysis voltage rather than pressure signals are compared.

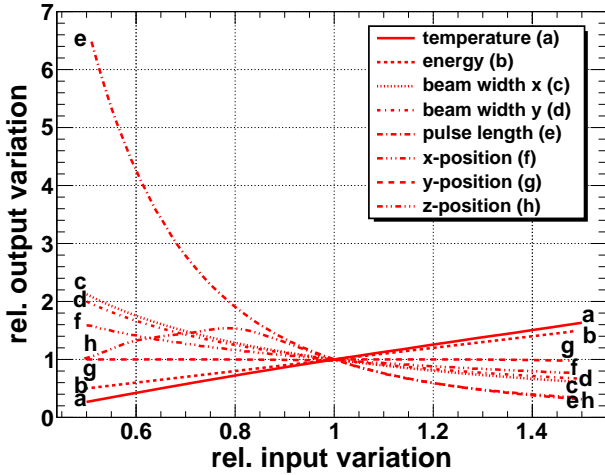
The shapes of the simulated pulses are altered by the sensor response, especially the high-frequency components above the resonant frequency of the sensor. In the case of the laser pulse, mostly the resonance of the sensor is excited, leading to a strong ringing. For the proton beam, the primarily bipolar shape is again prominent, whereas the laser pulse is segmented into the two parts described above. The direct pulse of the laser experiment exhibits a bipolar shape as well, albeit less symmetric than for the proton beam.

Figure 5 exemplifies the dependency of the signal amplitude on the input parameters of the simulation: water temperature, pulse energy, beam profile in  $x$  and  $y$ , pulse length and the position of the sensor. As nominal positions of the sensor  $x = 0.10$  m,  $y = 0.0$  m, and  $z = 0.22$  m were used. All parameters were varied by  $\pm 50\%$  around the value of the best agreement with measurement, i.e. the values used for the simulations of the signals shown in Fig. 4.

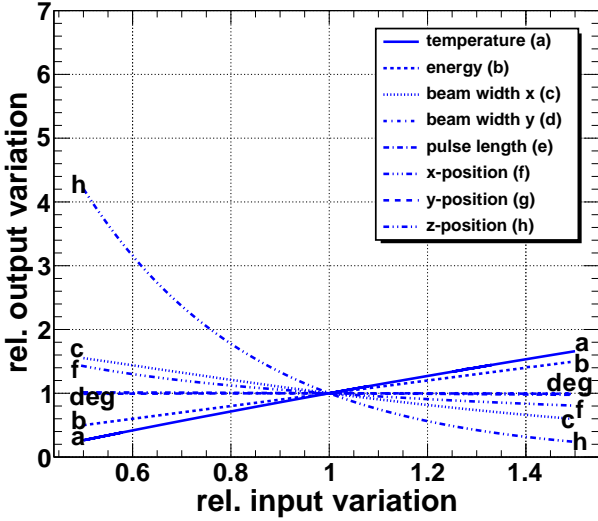
Some of the characteristics of thermo-acoustic sound gener-

ation are observable. As discussed in Sec. 2, the dependence on temperature enters through the factor  $v_s^2 \alpha / c_p$  (where the dependence on the speed of sound is negligible) and is roughly linear in the range investigated for this study. The dependence on energy is strictly linear. The dependency on the beam pulse parameters is diverse. It is governed by the integral in Eq. (10) and therefore depends on both the spatial and the temporal beam profiles and the interaction of the particles with the water. For a given point in space and time, the elementary waves produced in the volume of energy deposition may interfere constructively or destructively depending on the beam properties. Accordingly, the length of the laser pulse has no influence on the amplitude, as with 9 ns it is much shorter than the transit time of the acoustic signal through the energy deposition area. For the several ten  $\mu$ s long proton spill, the spill time is comparable to the transit time. Thus the acoustic signal shows a strong dependence on the spill time. The dependence on the radial coordinate  $r$  w.r.t. the beam axis  $r$  follows roughly the expected  $1/\sqrt{r}$  and  $1/r$  fall-off of a cylindrical source in the near and the far field, respectively. The  $y$ -position was varied between  $-2$  and  $2$  cm, as the signals were recorded within the  $xz$ -plane. The resulting change in amplitude is below 1%. The  $z$ -dependency for the laser experiment follows the exponential fall-off expected from the light absorption. The one for the proton experiment shows the only non-strictly monotonic behaviour due to the form of the energy deposition with the prominent Bragg peak.

Using these dependencies the systematic uncertainties of the model were obtained using the experimental uncertainties of the various parameters. The main uncertainty for the proton



(a) Proton beam simulation results



(b) Laser beam simulation results

Figure 5: Dependency of the simulated signal amplitude on variation of the simulation input parameters (labelled a - h) for the proton (upper graph) and the laser experiment (lower graph). With a nominal position  $y = 0$  m of the sensor, the full range of the variation corresponds to  $\pm 2$  cm for this parameter.

beam is given by the temporal profile of the pulse, which was simplified to a Gaussian profile for this chapter (however not for the rest of this work). For the laser beam experiment this parameter influences the signal amplitude only on a one percent level. The second main influence on the amplitude is the sensor position along the beam axis ( $z$ -direction).

Table 1 gives the parameters and their uncertainties ( $\Delta V$ ) used for the simulation of the signals. The resulting systematic uncertainties in the amplitude ( $\Delta A$ ) are given as well. The combined uncertainties are  $+34\%$  and  $-29\%$  for the proton signal and  $+26\%$  and  $-24\%$  for the laser signal, respectively.

Parameter	Proton		Laser	
	value ( $\Delta V$ )	$\Delta A$	value ( $\Delta V$ )	$\Delta A$
temperature	12.0°C ( $\pm 8\%$ )	+10% -11%	12.0°C ( $\pm 8\%$ )	$\pm 11\%$
energy	410 PeV ( $\pm 10\%$ )	$\pm 10\%$	520 PeV ( $\pm 10\%$ )	$\pm 10\%$
beam width (x-direction)	3.0 mm ( $\pm 14\%$ )	-14% +19%	5.0 mm ( $\pm 15\%$ )	-14% +16%
beam width (y-direction)	3.0 mm ( $\pm 14\%$ )	-12% +16%	5.0 mm ( $\pm 15\%$ )	$\pm 0\%$
pulse length	$1.0 \cdot 10^{-5}$ s ( $\pm 11\%$ )	-13% +16%	$6.9 \cdot 10^{-7}$ s ( $\pm 50\%$ )	-2% +2%
x-position	0.10 m ( $\pm 7\%$ )	-4% +5%	0.11 m ( $\pm 6\%$ )	-3% +4%
y-position	0.0 m ( $\pm 1$ cm)	-2% +0%	0.0 m ( $\pm 1$ cm)	-1% -1%
z-position	0.22 m ( $\pm 4\%$ )	$\pm 9\%$	0.17 m ( $\pm 5\%$ )	-11% +13%
combined		+34% -29%		+26% -24%

Table 1: Beam parameters used for the simulated signals in Fig. 4 with their associated experimental uncertainties ( $\Delta V$ ) and resulting uncertainty in signal amplitude ( $\Delta A$ ). The pulse length of the laser is set to a value much higher than in the experiment, to save calculation time. The resulting uncertainty in the signal amplitude is below 2%

## 6. Analysis Results

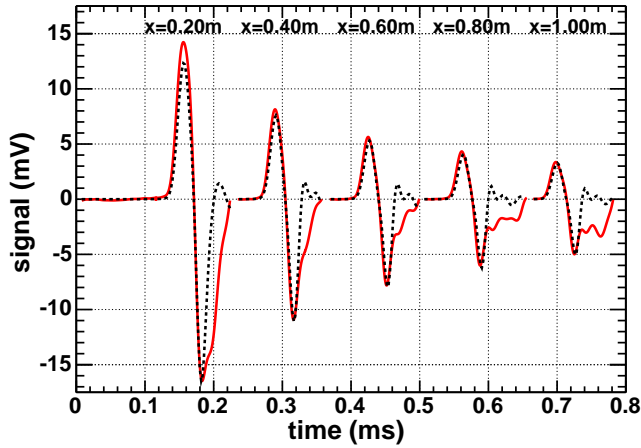
In the following, the results obtained in the comparison of experiment and simulation are presented.

### 6.1. Comparison of Simulated and Measured Signals

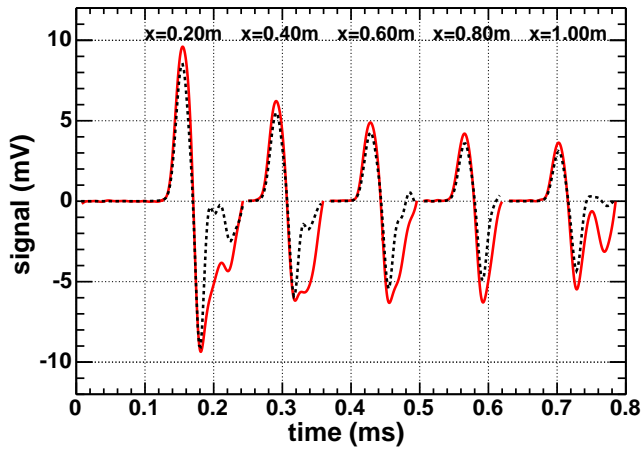
#### 6.1.1. Proton Beam Experiment

Figure 6 shows a comparison between simulated and measured signals for the proton beam experiment at different sensor positions.

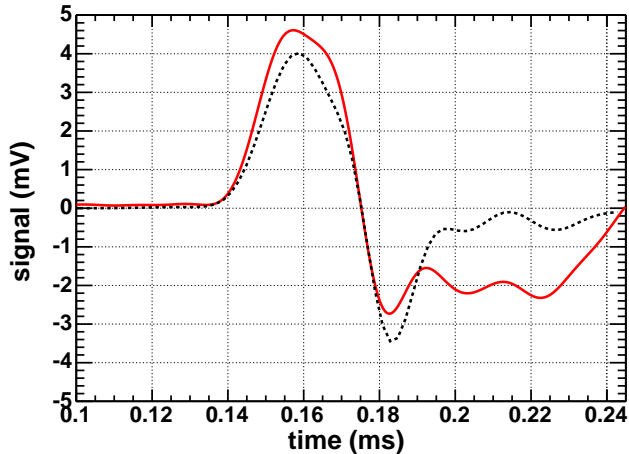
For better visibility only the main part of the signals (first bipolar part) is plotted. The input parameters of the simulation were varied within the experimental uncertainties until the best agreement with the measured signal in amplitude and duration was obtained for the reference point at  $x=0.40$  m and  $z=0.11$  m. For this optimisation, a simple procedure of adjusting the parameters manually and scanning the resulting agreement visually was found to be sufficient. The other signals were simulated with the same parameter set, only the sensor positions were changed. The signal shapes differ for different  $z$ -positions due to the geometry of the energy deposition profile described in Sec. 3 with cylindric form in the  $xy$ -plane and almost flat energy density in  $z$ -direction up to the Bragg peak at  $z=0.22$  m. Due to this geometry an almost cylindrical wave is excited in the medium, with coherent emission perpendicular to the beam axis. In the region  $z \lesssim 0.2$  m the signals are of bipolar shape. Along the beam axis ( $x \approx 0.0$  m,  $z > 0.25$  m) the main part of the observed signal originates from the Bragg peak as a nearly spheric source and no clear bipolar shape evolves.



(a) Signals at  $z = 0.11$  m



(b) Signals at  $z = 0.21$  m



(c) Signal at  $x = 0.01$  m,  $z = 0.41$  m

Figure 6: Comparison of measured (solid line) and simulated (dashed line) signals at different sensor positions for the proton beam experiment. Note the different scale of the  $x$ -axis used in plot (c). The reference signal for tuning the simulations is at  $z = 0.11$  m and  $x = 0.40$  m. The coordinate system is given in Fig. 1. See text for a detailed description.

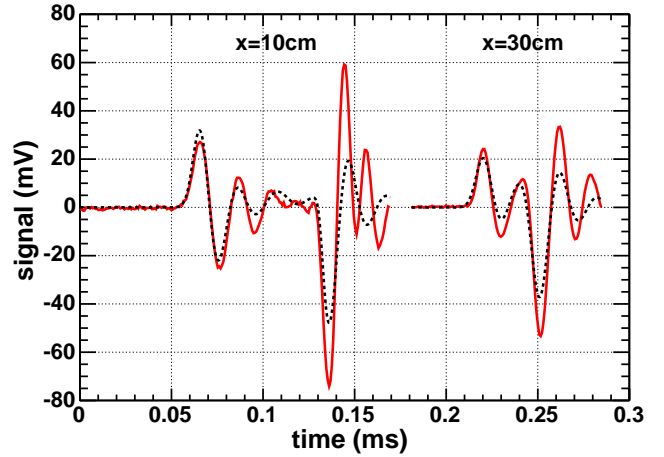


Figure 7: Comparison of measured (solid line) and simulated (dashed line) signals for the laser beam experiment at  $z = 0.17$  m for different sensor positions along  $x$  (reference at  $x = 0.10$  m). For more details see text.

The agreement between simulation and measurement is good for all positions. Not only amplitude and duration match (see also the following sections) but also the signal shape is reproduced to a very high degree. The small discrepancies, primarily in the rarefaction part of the bipolar pulse, have contributions stemming from a non-ideal sensor calibration and reflections on the tank surfaces. However, a significant part of the discrepancies may lie in the beam pulse modelling or even the thermo-acoustic model itself.

### 6.1.2. Laser Beam Experiment

The prominent feature of the energy deposition of the laser beam is at the beam entry into the medium. Overall, the geometry of this deposition is mainly a cylindrical one with rotational symmetry around the  $z$ -axis, as for the proton beam, with coherent emission perpendicular to the beam axis (direct signal). The signal from the discontinuity at the beam entry is emitted almost as from a point source (beam entry signal). In contrast to the proton beam, the shapes of signals at different positions along the  $z$ -axis do not vary much, only the relative timing between the two signal components varies. Therefore, Fig. 7 shows only signals for a  $z$ -position in the middle of the water tank. Here, both signal parts are well described by the simulation. The beam entry part of each signal is less well reproduced in the simulation due to its high frequency components where the sensor calibration is less well understood.

To compare the characteristics of the signals in simulation and measurement in the following studies, their amplitudes and the point in time of the recording of the signal maximum were further studied. For the laser signal, the direct signal part is considered only.

### 6.2. Speed of Sound Measurement

Equation (10) yields as velocity of propagation for the thermo-acoustic signal the speed of sound in the medium, here

water. To verify the hydrodynamic origin of the measured signals the variation of the arrival times for different sensor positions perpendicular to the beam axis were analysed. Figure 8 shows the measured data and a linear fit for each beam type. The data is compatible with an acoustic sound propagation in water, as the fits yield a speed of sound compatible with pure water at the temperature used. For the proton beam  $v_s = 1458 \pm 4$  m/s ( $\chi^2/\text{n.d.f.} = 8.2/11$ ) was obtained for a water temperature of  $11.0 \pm 0.2$  °C, where literature [16] gives for pure water at normal pressure  $v_s = 1455 \pm 1$  m/s which is in complete agreement<sup>3</sup>. For the laser measurements the water temperature of  $19.4 \pm 1.0$  °C and thus the speed of sound were significantly higher, the observed  $v_s = 1508 \pm 3$  m/s ( $\chi^2/\text{n.d.f.} = 9.2/13$ ) is again in perfect agreement with the theoretical value of  $1503 \pm 6$  m/s. The offset between proton and laser beam data in Fig. 8 is due to a differing delay time in between trigger time and arrival time of the different beams in the water and is irrelevant for the calculation of the speed of sound.

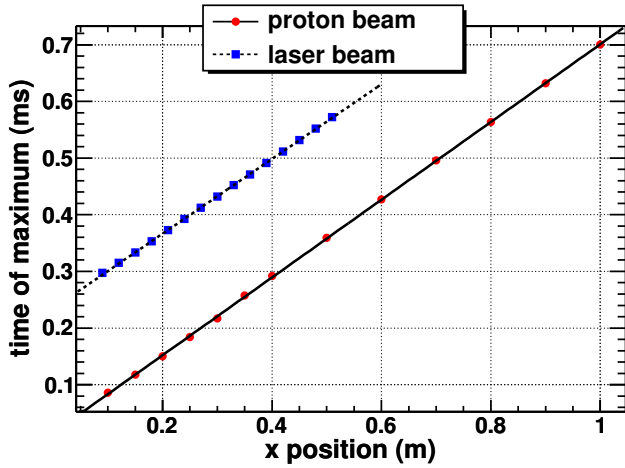


Figure 8: Arrival time of the signal maximum for different sensor position perpendicular to the beam ( $x$  position). The straight lines represent linear fits to the data points yielding  $v_s = 1458 \pm 4$  m/s and  $v_s = 1508 \pm 3$  m/s for the proton and laser beam, respectively.

### 6.3. Variation of the Sensor Position

The durations of the complete, unclipped signals vary with sensor positions mainly due to reflections, which were not simulated and can therefore not be compared.

The comparison of simulated and measured signals for different sensor positions within the water tank, excluding the parts of the signals dominated by reflections, was shown in Fig. 6. The good agreement between model and measurement also manifests itself in the development of the signal amplitude with distance of sensors from the beam axis, shown in Fig. 9. To minimise systematic effects from reflections, only the amplitude of the leading maximum is analysed.

<sup>3</sup>The uncertainties of the theoretical values of the speed of sound result from the changing water temperature while the measurements were taken.

Though there are sizeable deviations, the overall shape of the curve is reproduced. The behaviour is again different for the two  $z$ -positions. The development at  $z = 0.11$  m follows the one expected from a cylindrical source with a  $1/\sqrt{r}$  behaviour in the near field up to  $\sim 0.3$  m and a  $1/r$  behaviour in the far field beyond that distance. At the smallest measured distances, the simulated behaviour deviates from the measured one. Presumably this is due to simplifications made in the derivation of the model in Sec. 2. At  $z = 0.21$  m the amplitude falls off more uniformly, this is again a combination of the point-like emission characteristic of the Bragg peak interfering with the cylindrical emission at  $z < 0.2$  m.

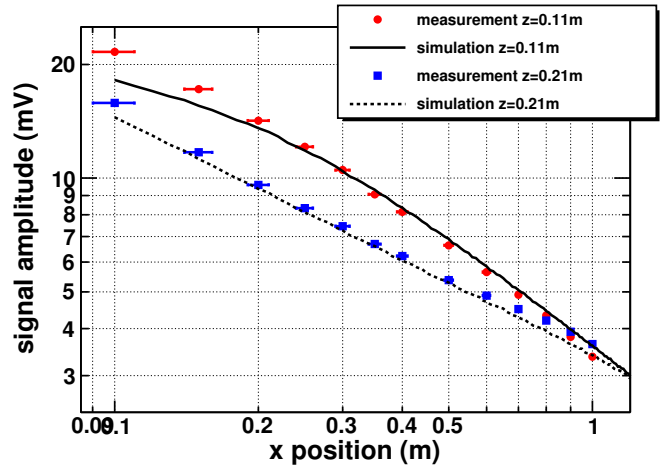


Figure 9: Development of the leading peak (maximum) with sensor position perpendicular to the beam axis ( $x$ ) for the proton beam experiment. Points mark the measured amplitudes for two different  $z$ -positions and the lines the respective simulation results.

The behaviour for the laser experiment is not as well reproduced by the simulation (see Fig. 10). This is again attributed to the high-frequent signal components of the laser, where minor uncertainties in the simulation may result in big changes of the signal amplitude. Especially the overlap of the direct with the beam entry window signal distort the signal shape. At distances exceeding 0.5 m the two signal parts cannot be distinguished.

### 6.4. Variation of the Pulse Energy

Assuming otherwise unchanged settings, the energy deposition density  $\epsilon$  scales linearly with total deposited energy. Thus the spill energy can be written as a pre-factor in Eq. (10) effecting the pressure and thus signal amplitude linearly. As shown in Fig. 11 this behaviour was observed in the experiments yielding a zero-crossing of the pulse energy at  $(-4.1 \pm 5.3)$  mPa for the proton beam and  $(42 \pm 87)$  mPa for the laser beam. Both values are consistent with zero. The slope of the line depends on the energy deposition and the sensor positioning along the beam axis and can therefore not be compared for the two beams. As expected from the model, the signal duration and signal shape showed no significant dependence on energy.

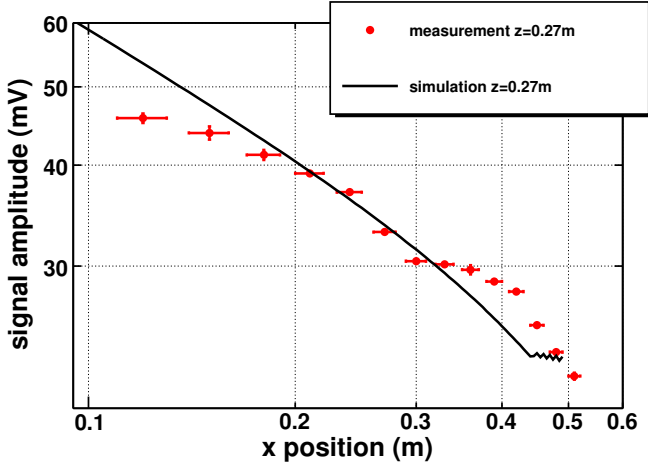


Figure 10: Development of the leading peak (maximum) with sensor position perpendicular to the beam axis ( $x$ ) for the laser beam experiment. Points mark the measured amplitudes at  $z = 0.27$  m and the line the simulation result.

### 6.5. Variation of the Temperature

The main feature of the thermo-acoustic model is its dependence on the temperature of the medium. Figure 12 shows the temperature dependence of the signal peak-to-peak amplitude for the laser beam, where a positive (negative) sign denotes a leading positive (negative) peak of the signal. The two data sets shown in the figure were recorded by two sensors simultaneously, which were positioned at  $x = 0.10$  m perpendicular to the beam axis and at  $z = 0.11$  m and  $z = 0.21$  m along the beam axis, respectively. In the case of the proton beam setup, which will be discussed below, these hydrophone positions correspond roughly to the  $z$ -position of the Bragg-peak and a  $z$ -position half way between the Bragg-peak and the beam entry into the water, respectively. For comparability, the same positions and the same sensors were chosen for the laser and proton beam experiments.

The laser beam signal shown in Fig. 12 changes its polarity around  $4^\circ\text{C}$ , as expected from the thermo-acoustic model. The theoretical expectation for the signal amplitude, which is proportional to  $\alpha/c_p$  and vanishes at  $4^\circ\text{C}$  for the given temperature and pressure, is fitted to the experimental data. In the fit, an overall scaling factor and a shift in temperature (for the experimental uncertainty in the temperature measurement) were left free as fit parameters. The fit yielded a zero-crossing of the amplitude at  $(3.9 \pm 0.1)^\circ\text{C}$ , where the error is dominated by the systematic uncertainty in the temperature setting.

Analysing the proton data in the same fashion resulted in a fit that deviated from the model expectation, and a zero-crossing significantly different from  $4.0^\circ\text{C}$  at  $(4.5 \pm 0.1)^\circ\text{C}$ , see Fig. 13. The data strongly indicate the presence of a systematic effect near the zero-crossing of the signal amplitude. To understand this effect, the signal shapes near the temperature of  $4.0^\circ\text{C}$  were investigated (Fig. 14). A non-vanishing signal is clearly observable at  $4.0^\circ\text{C}$  and the signal inverts its polarity between  $4.0^\circ\text{C}$  and  $4.5^\circ\text{C}$ . In view of the results from the laser beam measurements and the obvious systematic nature of the deviation from

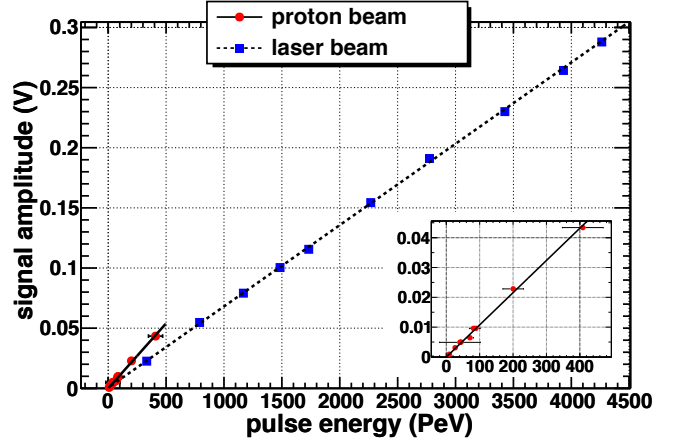


Figure 11: Peak-to-peak amplitude of signals for different pulse energies, for both beams the sensors were at a position  $x \approx 0.10$  m. There is a ten percent systematic uncertainty in the absolute determination of the pulse energy. The lines represent linear fits to the data points yielding a zero-crossing of the amplitude compatible with no energy in a pulse. The insert shows the data for the proton beam.

the model visible in Fig. 13, we subtracted the residual signal at  $4.0^\circ\text{C}$ , which has an amplitude of 5% of the  $15.0^\circ\text{C}$  signal, from all signals. Thus a non-temperature dependent effect in addition to the thermo-acoustic signal was assumed. The resulting amplitudes shown in Fig. 15 are well described by the model prediction.

The production mechanism of the underlying signal at  $4.0^\circ\text{C}$ , which was only observed in the proton experiment, could not be unambiguously determined with the performed measurements. From the model point of view, the main simplification for the derivation of Eq. (10) was to neglect all non-isotropic terms and momentum transfer to the medium in the momentum density tensor  $\Pi_{ij}^B$  by setting  $\beta = 0$  in Eq. (7). As discussed in Sec. 2, dipole radiation could contribute significantly near the disappearance of the volume expansion coefficient for the case  $\beta \neq 0$ . Also other non-thermo-acoustic signal production mechanisms have been discussed in the literature which could give rise to an almost temperature independent signal, see e.g. [2]. The obvious difference to the laser experiment are the charges involved both from the protons themselves and the ionisation of the water which could lead to an interaction with the polar water molecules. Another difference are the massive protons compared to massless photons. Residual signals at  $4.0^\circ\text{C}$  were found in previous works as well [4–6, 8], as will be discussed in more detail in Sec. 6.6.

For clarification further experiments are needed either with ionising neutral particles (e.g. synchrotron radiation) or with charged particles (e.g. protons,  $\alpha$ -particles) with more sensors positioned around the Bragg-peak. With such experiments it might be possible to distinguish between the effect of ionisation in the water and of net charge introduced by charged particles.

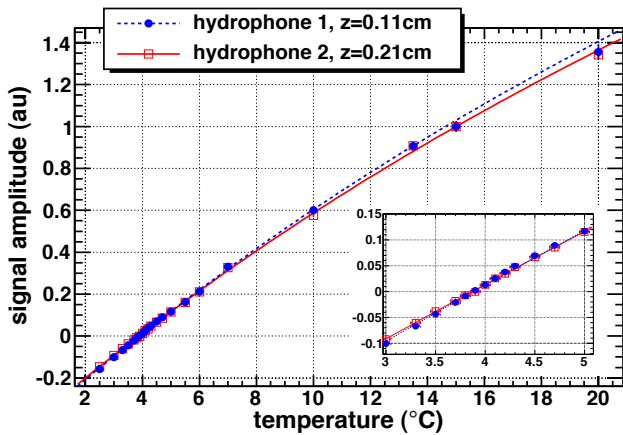


Figure 12: Measured signal amplitude of the bipolar acoustic signal induced by laser pulses at different temperatures fitted with the theoretical expectation as described in the text. All amplitudes were normalised to 1 at 15.0°C. The insert shows a blow-up of the region around 4°C where the sign of the amplitude changes.

### 6.6. Comparison with Previous Experiments

With the analysis that has been described above, the signal production according to the thermo-acoustic model could be unambiguously confirmed. While the model has been confirmed in previous experiments, the simulations presented in this work constitute a new level of precision. The most puzzling feature, a residual signal at 4°C that was also observed in previous experiments, was investigated with high precision by scanning the relevant temperature region in steps of 0.1°C. The observed shift of the zero-crossing of the amplitude towards values higher than 4°C, caused by a leading rarefaction non-thermal residual signal at 4°C, is in qualitative agreement with [5]. In [4], a residual signal at 4°C was also reported. Since in that work the zero-crossing of the amplitude is observed at 6°C, i.e. a higher value than the expected 4°C, it can be assumed that the corresponding residual signal has a leading rarefaction.

In [8], a residual signal is found at 4.25°C, however with a leading compression rather than rarefaction. The authors conclude that this may lead to a signal disappearance point *below* the expected value, in contrast to [4, 5] and the work presented in this article.

For the measurements with a laser beam reported in [6], a residual signal was also observed at 4°C, albeit with a leading compression and a subsequent reduction of the temperature of the zero-crossing of the signal amplitude to about 2.5° – 3.0°C. This observation is in contrast to the laser experiment presented in this article.

In conclusion, the works of all authors discussed here indicate a non-thermal residual signal for proton beams, albeit with varying results concerning the size of the effect and the shape of the underlying non-thermal signal. The results for the laser beam reported in [6] differ from those described in the article at hands. It should be pointed out, however, that in [5] and [6] results are reported by the same authors for proton and for

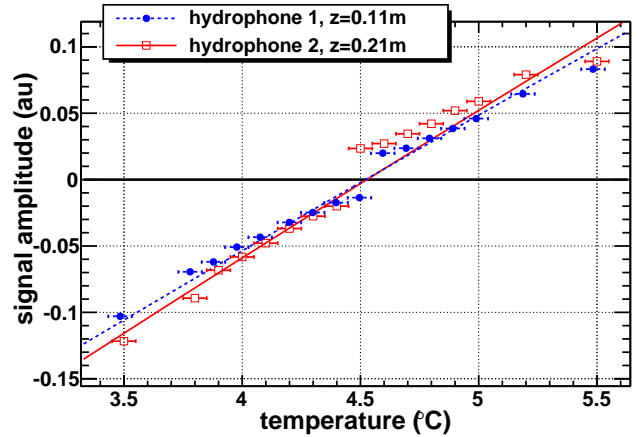


Figure 13: Measured signal amplitude of the bipolar acoustic signal induced by proton pulses at different temperatures near 4.0°C, fitted with the model expectation as described in the text. A systematic deviation from the model expectation as the amplitude changes its sign is clearly visible. The amplitudes were normalised to 1 at 15.0°C.

laser beams, respectively. A comparison of these two publications shows that a different behaviour near the temperature of 4°C was observed for the two types of beams. Hence, to the best of our knowledge, there are currently no results in contradiction with the notion of different non-thermal effects in the interaction of proton vs. laser beams with water. The available data does not allow for a more detailed analysis of the correlation between experimental conditions and the temperature of the zero-crossing of the signal amplitude.

## 7. Applications in Astroparticle Physics

Efforts to detect neutrinos at ultra-high energies are at the frontier of research in the field of astroparticle physics. Neutrinos are the only viable messengers at ultra-high energies beyond the local universe, i.e. distances well beyond several tens of Megaparsecs. If successful, the investigation of these elusive particles will not only enhance the understanding of their own nature, but also provide important complementary information on the astrophysical phenomena and the environments that accelerate particles to such extreme energies.

For acoustic particle detection, not only the technical aspects such as optimal design and detector layout are subject of research. But also the underlying physics processes—i.e. the formation of hadronic cascades resulting from neutrino interactions in dense media—have never been observed directly in detector experiments at these energies. Producing ever more reliable extrapolation of reaction properties to ultra-high energies is an ongoing effort. With advancements in the simulations of cascades forming in water and improvements of detector simulation tools, the discrepancy between cascade parameters from independent simulations decreased: recent studies differ only slightly [17, 19–21]. At the same time it is necessary to gain a solid understanding of the sound signals generated from the energy depositions by particle cascades. For this purpose, laboratory measurements are required.

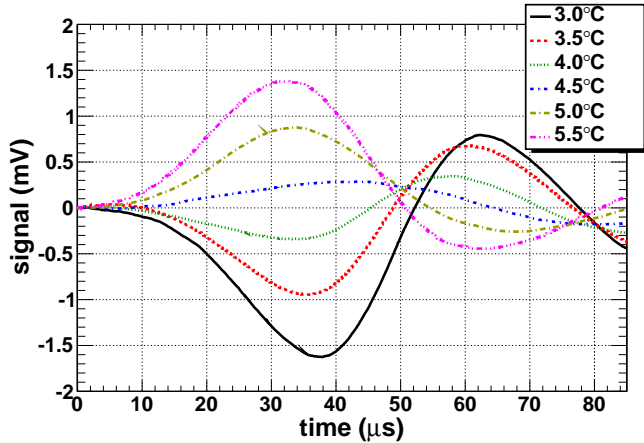


Figure 14: Comparison of signals recorded for the proton beam with hydrophone 1 at different temperatures. For each temperature, the signals were first smoothed with a 100 kHz second order Butterworth low pass filter. Subsequently 1000 waveforms were averaged, as described in Sec. 3. To allow for an easy comparison of the signal shapes, a point in time at the onset of the acoustic signals was chosen as zero time and for all signal amplitudes the corresponding offset was added or subtracted to yield a zero amplitude at that time.

This work, together with others [4–8, 22, 23] has established the validity of the thermo-acoustic model with uncertainties at the 10% level. The input to a model as discussed in this article is an energy deposition in water as it is also produced by a cascade that evolves from a neutrino interaction. In comparison with the uncertainty in the thermo-acoustic model, uncertainties due to the simulations of hadronic cascades and cascade-to-cascade variations are large [19], dominating the challenge to detect and identify sound signals resulting from neutrino interactions. It can hence be concluded that the current level of precision in modelling sound signals in the context of the thermo-acoustic model is fully sufficient for the understanding of acoustic neutrino signatures. The latter is necessary to improve the selection efficiency and background rejection for neutrino detection algorithms in potential future acoustic neutrino detectors. Several experiments have been conducted [21, 24–26] to understand the acoustic background at the sites of potential future large-scale acoustic neutrino telescopes in sea water, fresh water and ice. The combination of simulation efforts, laboratory measurements and studies with in-situ test arrays will allow for a conclusion of the feasibility of acoustic neutrino detection.

## 8. Conclusions

We have demonstrated that the sound generation mechanism of intense pulsed beams is well described by the thermo-acoustic model. In almost all aspects investigated, the signal properties are consistent with the model. The biggest uncertainties of the experiments are on the 10% level. One discrepancy is the non-vanishing signal at 4°C for the proton beam experiment, which can be described with an additional non-temperature dependent signal with a 5% contribution to the amplitude at 15°C. The model allows for calculations of the characteristics of sound pulses generated in the interaction of high

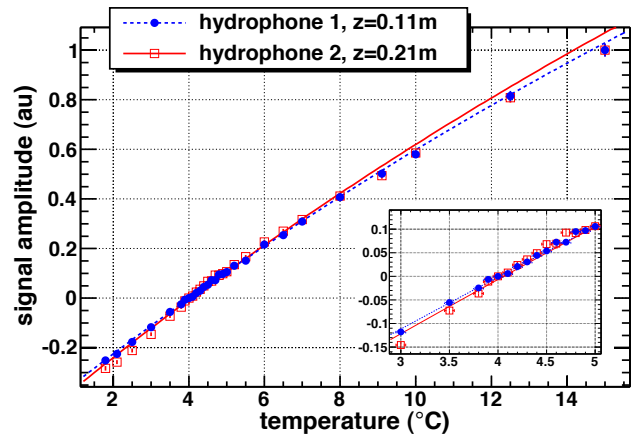


Figure 15: Measured signal amplitude of the bipolar acoustic signal induced by proton pulses at different temperatures fitted with the model expectation as described in the text. The non-thermo-acoustic signal at 4.0°C was subtracted at every temperature. The amplitudes were afterwards normalised to 1 at 15.0°C. The insert shows a blow-up of the region around 4°C where the sign of the amplitude changes.

energy particles in water with the input of the energy deposition of the resulting cascade. A possible application of this technique would be the detection of neutrinos with energies  $\gtrsim 1$  EeV.

## Acknowledgements

This work was supported by the German ministry for education and research (BMBF) by grants 05CN2WE1/2, 05CN5WE1/7 and 05A08WE1. Parts of the measurements were performed at the “Theodor Svedberg Laboratory” in Uppsala, Sweden. The authors wish to thank all involved personnel and especially the acoustics groups of DESY Zeuthen and of Uppsala University for their support.

## References

- [1] G.A. Askaryan, *Atomnaya Energiya* **3**, 152 (1957).
- [2] G.A. Askaryan et al., *Nucl. Inst. Meth.* **164**, 267 (1979).
- [3] J.G. Learned, *Phys. Rev. D* **19**, 3293 (1979).
- [4] L. Sulak et al., *Nucl. Inst. Meth.* **161**, 203 (1979).
- [5] S.D. Hunter et al., *J. Acoust. Soc. Am.* **69(6)**, 1557 (1981).
- [6] S.D. Hunter et al., *J. Acoust. Soc. Am.* **69(6)**, 1563 (1981).
- [7] V.I. Albul et al., *Instr. Exp. Tech.* **44**, 327 (2001).
- [8] V.I. Albul et al., *Instr. Exp. Tech.* **47**, 507 (2004).
- [9] A. Roberts, *Rev. Mod. Phys.*, **64(1)**, 259 (1992).
- [10] A. Achterberg et al. (IceCube Collaboration), *Astropart. Phys.* **26(3)**, 155 (2006).
- [11] M. Ageron et al. (ANTARES Collaboration), *Nucl. Instrum. Methods A* **656**, 11 (2011).
- [12] A. Avrorin et al. (Baikal Collaboration), *Nucl. Instrum. Methods A* **626-627**, S13 (2011).
- [13] R. Engel et al., *Phys. Rev. D* **64(9)**, 093010 (2001).
- [14] S. Agostinelli et al., *Nucl. Instrum. Methods A* **506(3)**, 250 (2003).
- [15] L.D. Landau and E.M. Lifschitz, *Course of Theoretical Physics, Vol.6: Fluid Mechanics*, Pergamon Press, London, 2nd Edition (1987).
- [16] V. A. Del Grosso and C. W. Mader, *J. Acoust. Soc. Am.* **52(5B)**, 1442 (1972).

- [17] S. Bevan et al., *Astropart. Phys.* **28(3)**, 366 (2007)
- [18] G. Anton et al., *Astropart. Phys.* **26(4-5)**, 301 (2006)
- [19] S. Bevan et al., *Nucl. Instrum. Methods A* **607**, 398 (2009).
- [20] V. Niess and V. Bertin, *Astropart. Phys.* **26(4-5)**, 243 (2006)
- [21] J. Vandenbroucke et al., *Astrophys. J.* **621**, 301 (2005)
- [22] A. Capone and G. de Bonis, *Int. J. Mod. Phys. A* **21(S1)**, 112 (2006)
- [23] V.S. Demidov et al., *Int. J. Mod. Phys. A* **21(S1)**, 122 (2006)
- [24] S. Böser et al., *Int. J. Mod. Phys. A* **21(S1)**, 221 (2006)
- [25] G. Riccobene, *Nucl. Instrum. Methods A* **602(1-2,S1)**, 149 (2009)
- [26] J.A. Aguilar et al. (ANTARES Collaboration), *Nucl. Instrum. Methods A* **626-627**, 128 (2011)